



## **AIAA 2002-0275**

# **Recent Applications and Improvements to the Engineering-Level Aerodynamic Prediction Software MISL3**

D. Lesieutre, J. Love, and M. Dillenius  
Nielsen Engineering & Research, Inc.  
Mountain View, CA

A. B. Blair, Jr.  
Williamsburg, VA

**40th AIAA Aerospace Sciences  
Meeting & Exhibit**  
14-17 January 2002 / Reno, NV

For permission to copy or republish, contact the copyright owner named on the first page.

For AIAA-held copyright, write to AIAA Permissions Department,  
1801 Alexander Bell Drive, Suite 500, Reston, VA, 20191-4344.

## RECENT APPLICATIONS AND IMPROVEMENTS TO THE ENGINEERING-LEVEL AERODYNAMIC PREDICTION SOFTWARE *MISL3*

Daniel J. Lesieutre<sup>\*</sup>, John F. Love<sup>†</sup>, Marnix F. E. Dillenius<sup>‡</sup>  
Nielsen Engineering and Research, Inc.  
Mountain View, CA 94043

A.B. Blair, Jr.<sup>§</sup>  
Williamsburg, VA

### ABSTRACT

Engineering-level missile aerodynamics prediction code *MISL3* has recently been applied to a variety of configurations including two tandem-control models and to a two-fin-set model with free rolling tail fins tested at NASA Langley Research Center. Enhanced capabilities since the earlier *M3HAX* version include the modeling of conical changes in body diameter (flares, boattails) and arbitrary interdigitation angles between fin sets. Results presented include high angle of attack aerodynamics, induced lateral forces, tandem-control fin deflections, configurations with flares and/or boattails, estimates of free rotating fin section performance, rotational damping estimates, and updates to results presented in an earlier paper. Comparisons to independent experimental data are presented to demonstrate the unique qualities of the code. In general, good agreement with experimental data is obtained for a variety of configurations (body alone, single-fin set, two-fin set, and three-fin set configurations) and flow conditions (symmetric and asymmetric).

### LIST OF SYMBOLS

a	body radius at fin mid-rootchord
AR	aspect ratio (two fins joined at root)
$C_{dc}$	body crossflow drag coefficient
$C_l$	rolling moment/ $q_\infty S_R l_R$
$C_{lp}$	roll-damping coefficient; $\partial C_l / \partial (p l_R / 2 V_\infty)$
$C_m$	pitching moment/ $q_\infty S_R l_R$ ; positive nose up
$C_N$	normal force/ $q_\infty S_R$
$C_{NF}$	fin normal force/ $q_\infty S_R$
$C_{N\alpha}$	body $dC_N/d\alpha$ at $\alpha=0$
D	body diameter, maximum
L	body length
$l_R, l_{REF}$	reference length

<sup>\*</sup> Senior Research Engineer, Senior Member AIAA

<sup>†</sup> Research Engineer

<sup>‡</sup> President, Associate Fellow AIAA

<sup>§</sup> Aerospace Technologist, Associate Fellow AIAA

p,q,r	rotational rates, rads/sec
s	exposed fin span
$s_m$	fin semispan measured from body centerline
$S_R$	reference area
$x_{CP}$	center of pressure
$x_{MC}$	moment center
$\alpha_c$	included angle of attack, deg
$\delta$	fin deflection angle, deg
$\lambda$	fin taper ratio
$\phi$	roll angle, deg
$\phi_{F2}$	interdigitation angle of fin set 2 (tail) with respect to the first fin section, deg

### INTRODUCTION

The engineering-level missile aerodynamic prediction code *MISL3*<sup>1</sup> (earlier versions are *M3FLR*, *M3HAX*,<sup>2,3</sup> *M3F3CA*,<sup>4</sup> earlier *MISL3*,<sup>5</sup> *MISSILE3*<sup>6</sup>) has been developed for aerodynamic performance prediction and for preliminary design of conventional missiles. The method uses the Triservice systematic fin-on-body force and moment data base<sup>4,7</sup> which covers a Mach number range from 0.6 to 4.5, fin aspect ratios from 0.25 to 4.0, angles of attack up to  $\pm 45^\circ$ , arbitrary roll angles, and deflection angles from  $-40^\circ$  to  $40^\circ$ . The method uses the equivalent angle of attack concept which includes the effects of vorticity and geometric scaling. The latest program described here is designated *MISL3*.<sup>1</sup> Program *MISL3* has been developed by extending the previous codes to model conical changes in body diameter (flares, boattails) and to allow arbitrary interdigitation angles between fin sets. This, in combination with the roll rate capability of the code, allows estimation of the performance of configurations with rolling fin sets. In addition, the paper publishes experimental data for a Tandem-Control model tested by co-author Blair (now retired) at NASA Langley Research Center (NASA/LARC). Predicted results from *MISL3* are compared to these data.

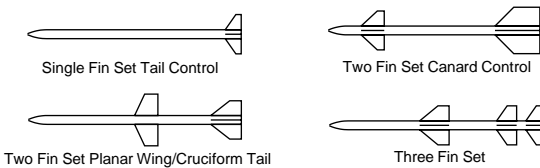
The range of parameters allowed by program *MISL3* is summarized in Table 1 below.

Flow Conditions:  
 $0.5 \leq M_\infty \leq 5.0$      $-90^\circ \leq \alpha_c \leq 90^\circ$   
arbitrary roll angle  $\phi$      $-40^\circ \leq \delta \leq 40^\circ$   
arbitrary rotational rates (p,q,r)  
user-specified nonuniform flow field

Geometries:  
 $0.25 \leq AR \leq 10.0$      $0.0 \leq \lambda \leq 1.0$   
up to three finned sections    1 to 4 fins per finned section  
identical fins within a section    symmetrical airfoil sections  
no fins with forward sweep    no fin trailing edge sweep  
arbitrary interdigitation between fin sets

Table 1. Range of Parameters

Some examples of configurations addressable by *MISL3* are shown in the next sketch.



The technical approach section of this paper summarizes the calculation procedures included in the *MISL3* program and describes the recent modeling improvements. The experimental and analytical data bases used within the *MISL3* program are described in Refs. 3 and 7. Extensive comparisons are presented to independent experimental data for a variety of configurations and flow conditions, and conclusions and acknowledgements are given.

### TECHNICAL APPROACH

This section summarizes body and fin force and moment calculations and describes recent improvements to the methodology employed in *MISL3*.

### BODY FORCE AND MOMENT CALCULATIONS

This section describes the body load calculation. *MISL3* improves the body modeling of *M3HAX*<sup>2,3</sup> by allowing conical changes in body diameter (flares and/or boattails). The potential and crossflow drag approach described in Ref. 2 is employed and summarized here. To determine the loads acting on the body, the body is divided into segments. The load on each segment,  $i$ , is determined including effects due to freestream, angular rates, and nonuniform flow fields. Potential normal force contributions are computed whenever  $dr_i/dx$  or  $d\alpha_i/dx$  are nonzero. The body radius slope  $dr_i/dx$  will be nonzero on the body nose and on any flares or boattails. The axial variation in local flow angle of

attack or sideslip will be nonzero whenever there are rotational rates or nonuniform flow field effects.

### Angular Rates and Nonuniform Flow Field Effects.

In order to include the effects of angular rates and a nonuniform flow field, the body is divided into nose, flare/boattail, fin, and afterbody sections. Each of these sections is divided into segments. Control points are fixed at the midpoints of each segment (on the centerline of the body). The local velocity induced by the angular rates is found for each segment control point by taking the cross product of the rotational rate vector (p,q,r) and the body control point position vector as measured from the rotation center. Normalized perturbation velocities at the body segment control points from a nonuniform flow field are added to the normalized angular rate induced velocities. The nonuniform flow field velocities are user-supplied. Forces and moments are calculated for each segment along the length of the body using the differential form of the equations developed by Jorgensen<sup>8</sup> shown below.

Potential Component of Body Load Calculation. The potential part of the normal force on the body is given in differential form by:

$$\frac{dC_N}{dx} = \frac{C_{N\alpha}}{2} \left[ \frac{r_i^2}{r_b^2} \frac{d\alpha_i}{dx} \left( -\frac{1}{2} \sin 2\alpha_i \sin \frac{\alpha_i}{2} + 2 \cos \frac{\alpha_i}{2} \cos 2\alpha_i \right) + 2 \frac{r_i}{r_b^2} \frac{dr_i}{dx} \sin 2\alpha_i \cos \frac{\alpha_i}{2} \right] \quad (1)$$

where  $r_i$  is the body radius at the control point,  $r_b$  is the radius of the missile base,  $dr_i/dx$  is the body slope at the control point, and  $\alpha_i$  is the local angle of attack for the segment determined from the sum of the freestream, angular, and nonuniform flow field velocities normal to the missile centerline. A similar equation can be written for the potential side force. Lift curve slope  $C_{N\alpha}$  is user input (usually set equal to 2.0).

### Crossflow Drag Component of Body Load Calculation.

If the freestream angle of attack is greater than  $4^\circ$ , the flow may separate. The axial location of the point of separation is determined from empirical relationships.<sup>5</sup> The crossflow drag contribution to normal force, in differential form, is calculated as follows for all control points aft of the point of separation:

$$\frac{dC_N}{dx} = 2\eta \frac{C_{dc}}{\pi} \frac{r_i}{r_b^2} \left[ \left( \frac{w_i}{V_\infty} \right)^2 + \left( \frac{v_i}{V_\infty} \right)^2 \right]^{1/2} \frac{w_i}{V_\infty} \quad (2)$$

where  $C_{dc}$  is the crossflow drag coefficient<sup>2,8</sup> and  $\eta$  is a correction factor for finite body length.<sup>2,9</sup> Both are a function of crossflow Mach number,  $M_\infty \sin \alpha_c$ . To compare to sting-mounted wind tunnel models, the correction factor  $\eta$  should be set to 1.0.

### **FIN FORCE AND MOMENT CALCULATION**

This section summarizes the fin force and moment calculation and the equivalent angle of attack methodology. References 2 and 3 provide a complete description of this methodology. The primary improvement in the new *MISL3* code is the ability to handle arbitrary interdigitation angles between fin sets. This modification affects the orientation of aft fin sets to upstream vorticity and the resolution of predicted forces into the appropriate coordinate systems.

### **VORTEX MODELING IN MISL3**

There are three nonlinear vortex models contained in *MISL3*.<sup>1-4</sup> The forebody vortex model is used to obtain the vortex field influencing the first fin set. A fin vortex model is required to shed the vorticity from upstream fin sets which influence the loads on aft fin sets, and an afterbody vortex shedding model is required to shed and track all vorticity along the body between fin sets. These models are described in detail in Refs. 2 through 4. For *MISL3*, the body vortex shedding and tracking model has been modified to include the effects of the nonuniform flow field and rotational rates. This amounts to including a doublet term which accounts for the local nonuniform flow and rotational rate effects at each body segment. In addition, two-dimensional sources/sink have been added to the vortex tracking procedure to ensure that vortices are pushed out over an expanding flare section and pulled in over a decreasing radius flare/boattail section. An example of a vortex field obtained with the *MISL3* code is shown in the results section.

### **AXIAL FORCE PREDICTION**

The axial force prediction methodology in *MISL3* is semi-empirical and has been described previously.<sup>2,4</sup> The following components contribute to the overall axial force: skin friction, subsonic pressure, transonic pressure/wave, supersonic wave, body base, fin trailing edge base, fin deflection, and angle of attack induced.

## **RESULTS**

This section presents longitudinal and lateral-directional aerodynamic predictions obtained with the *MISL3* prediction software. Comparisons of the results to

experimental data are made for a variety of configurations, including: body-alone, single-fin set, two-fin set, and three-fin set configuration. In addition, the capability of *MISL3* to predict lateral-directional aerodynamic characteristics for asymmetric flow conditions and fin deflections is also illustrated. Comparisons of predictions to the Tandem-Control Model data base are presented. The effects of interdigitation between fin sets is analyzed along with the estimation of tail fin section roll rate for a canard-tail configuration with a free-rolling tail section.

Results are also presented for several configurations presented originally in Ref. 10. In that reference, results were obtained with *M3FLR*. The results shown in this paper reflect corrections to geometry input, body lift curve slope  $C_{N\alpha}$  (Eqn. 1), and crossflow drag correction factor  $\eta$  (Eqn. 2). Unless otherwise noted,  $C_{N\alpha} = 2.0$  and  $\eta = 1.0$  for all predicted results.

### **BODY-ALONE, 4 TAIL FINS, 8 TAIL FINS, AND AFT FLARE CONFIGURATIONS**

Figure 1 compares predicted and measured<sup>11</sup> results for four configurations: 1) cone-cylinder, 2) cone-cylinder with four tail fins, 3) cone-cylinder with eight tail fins, and 4) cone-cylinder with a flare. In *MISL3*, the eight tail fin configuration is approximated by superimposing two (2) cruciform fin sets on top of one another with one set rotated 45° from the other. Overall normal force, pitching moment, axial force, and center of pressure are shown. The increments in aerodynamic characteristics between these configurations are predicted reasonably well. The normal force on the cone-cylinder-flare configuration is overpredicted; it is underpredicted at low angles of attack for the three other configurations. The axial force is predicted well.

### **SINGLE-FIN SET CONFIGURATION**

Predicted and measured<sup>12</sup> results are presented in Figures 2, 3, and 4 for a body-tail configuration with a small boattail. The body consists of a 3-caliber ogive nose, a 9.53-diameter cylindrical body, and a 0.53-diameter 4° boattail section. The tail fins have a body radius to fin semispan ratio,  $a/s_m$ , of 0.4, an aspect ratio of 1.52, and a taper ratio of 0.42.

*MISL3* (formerly *M3FLR*) results for this configuration were presented first in Ref. 10. These results were influenced by a fin geometry error and by the body force calculation parameters,  $C_{N\alpha}$  and  $\eta$ .

Figure 2 depicts measured and predicted results for  $\phi = 0^\circ$ , Mach numbers of 1.60 and 2.86, and tail pitch

deflections of 0 and 10°. The normal force characteristics are predicted reasonably well. There is an underprediction in the moderate angle of attack range, 5 to 15°. The pitching moment characteristics are predicted well with a maximum center of pressure difference of approximately one body radius. The axial force characteristics are predicted well.

Figure 3 shows measured and predicted results for a Mach number of 2.86, a roll angle of 45°, and pitch deflection of 0 and 10°. The results are similar to the  $\phi = 0^\circ$  results. The normal force is underpredicted in the moderate angle of attack range. The center of pressure is within 0.75 body radius, and the axial force is predicted well.

Figure 4 shows measured and predicted tail fin loads  $M_\infty = 2.86$  with 0 and 10° pitch deflection. Results are shown for three fin positions: 1) 45° to the leeward side, 2) horizontal position, and 3) 45° to the windward side. The results for the fin in the 45° to leeward position are in excellent agreement with the measured results. The nonlinearity in fin loads for this position are due to body vortices on the leeward-side of the body. The horizontal and windward position results agree well for zero deflection but are underpredicted for 10° pitch control.

### **SINGLE-FIN SET CONFIGURATION WITH BOATTAILS**

Predicted and measured<sup>13</sup> results are presented in Figures 5 and 6 for body-tail configurations with and without boattails. The body consists of a 0.62-caliber blunted cone nose and a total afterbody length 6.01 diameters based in the maximum body diameter. For the two configurations with boattails, the cylindrical center body is 3.01 diameters and the boattail section is 3.00 diameters. The ratio of the base diameter to the maximum diameter is 0.75 and 0.55 for the boattail configurations.

Figure 5 depicts results for the cylindrical afterbody (no boattail) with and without tail fins. Results are shown for  $\phi = 0^\circ$  and Mach numbers of 1.57 and 2.86. The trends of the aerodynamic characteristics are predicted, but the magnitudes are underpredicted for this configuration.

Figure 6 depicts the increment in normal force and pitching moment due to the two body boattail configurations with tail fins relative to the cylindrical afterbody configuration with fins. Also shown in Figure 6 is the comparison of axial force for the three tail fin configurations as a function of Mach number.

The axial force is predicted well. The effects of the boattails are predicted well by *MISL3*.

### **THREE-FIN SET CONFIGURATION WITH BODY FLARES AND INTERDIGITATION**

Figure 7 shows the three-fin-set configuration of Ref. 14. The body consists of a blunt nose shape followed by a cylindrical body section with a cruciform first fin section. Aft of the first fin set there is a small flare section followed by a cylindrical body section. There is a second flare section immediately in front of the second fin set. The second fin set is on a cylindrical body section. This is followed by a larger flare section and another cylindrical body section. A third fin set is located at the base. The second and third fin sets are interdigitated 45° relative to the first set. The planform shape of fins in fin sets 1 and 2 were idealized to satisfy the zero trailing-edge sweep constraint in *MISL3*. Predicted and measured<sup>14</sup> results for a Mach number of 1.82 are shown in Figure 7. Overall normal force, pitching moment, center of pressure, and axial force are shown. In general, the results indicate good agreement with the measured data. The center of pressure is predicted to within a body diameter. Some of the axial force characteristics with angle of attack are not predicted as well.

### **PLANAR HIGH-AR WING, HORIZONTAL TAIL, SINGLE VERTICAL TAIL CONFIGURATION**

Figure 8 shows measured<sup>15</sup> and predicted results for a configuration consisting of a high aspect ratio planar wing (AR = 4.76), horizontal tail surfaces (AR = 3.64), and a single vertical tail mounted on an ogive cylinder body. Details are given in Ref. 15. Overall normal force, axial force, and center of pressure are shown for a Mach number of 0.6. This configuration exercises several extensions within *MISL3*: 1) high aspect ratio, 2) high angle of attack, and 3) the ability to model less than four fins per fin set. The normal force and center of pressure are predicted well by *MISL3* with some underprediction in the 20° to 40° angle of attack range. The axial force is predicted reasonably well with the exception at 10° and above 45°.

### **TWO-FIN SET CONFIGURATION, TANDEM CONTROL**

**Tandem-Control Model Experiment.** Tandem-Control data presented in this section were obtained from tests conducted in the NASA/LaRC Unitary Plan Wind Tunnel at free-stream Mach numbers from 1.75 to 2.86.<sup>16</sup> The test objective was to provide an aerodynamic database to study and evaluate tandem

control as a concept and to exercise aerodynamic prediction codes on a generic canard and/or tail controlled research missile model. Test data included both canard and tail surfaces that operated either separately or together with only pitch control deflection settings.

The model had a tangent-ogive nose of fineness ratio 3.0, a smooth cylindrical body, and cruciform inline canards and aft tail fins. Tests were performed on two models. Both models had the same canard fins. The first model had larger span tail fins, and the second model had smaller tail fins identical to the canard fins. Model aerodynamic forces and moments were measured with an internally mounted six-component strain-gage balance. To assure turbulent flow over the model all tests were performed with boundary-layer transition strips located on the model nose and near the leading edges of the canard and tail fins. The test Reynolds number was 2.0 million per foot.

Figure 9 shows measured and predicted<sup>16</sup> results for the Tandem-Control Model described above. The model consists of a 3-caliber ogive nose followed by a 12-caliber cylinder. The canards fins have an aspect ratio of 1.6 and a taper ratio of 0.625; the tail fins have an aspect ratio of 2.33 and a taper ratio of 0.625. Both the canards and tails can be deflected. Figure 9 depicts the configuration and presents results for  $M_\infty = 1.75$  and  $\phi = 0^\circ$ . Results are shown for four sets of horizontal fin deflections:

- 1)  $\delta_{\text{CANARD}} = 0^\circ, \delta_{\text{TAIL}} = 0^\circ$
- 2)  $\delta_{\text{CANARD}} = 10^\circ, \delta_{\text{TAIL}} = 5^\circ$
- 3)  $\delta_{\text{CANARD}} = 10^\circ, \delta_{\text{TAIL}} = 10^\circ$
- 4)  $\delta_{\text{CANARD}} = 5^\circ, \delta_{\text{TAIL}} = -5^\circ$

The zero deflection case is a reference. Cases 2) and 3) are deflections for translation, and Case 4) is deflection for rotation in pitch. The normal force, pitching moment, center of pressure, and axial force are all predicted very well by *MISL3*. The nonlinear characteristics of the pitching moment are predicted by *MISL3*, and the center of pressure predicted is within a body radius of the measured values. The axial force characteristics are also predicted well.

Figure 10 shows measured and predicted<sup>16</sup> results for the Tandem-Control model described above. The results in Figure 10 are for the configuration with canard and tail fins which are identical; aspect ratio of 1.6 and a taper ratio of 0.625. Figure 10 depicts the configuration and presents results for canard pitch control for  $M_\infty = 1.75$  and  $\phi = 45^\circ$ . This case is shown because of the nonlinearities in the pitching moment which arise in

the “X” orientation from canard vortices affecting the tail fins. *MISL3* does a good job of predicting the nonlinear pitching moment characteristics, and predicts the overall center of pressure to within a body radius for this configuration.

Figure 11 shows measured and predicted<sup>16</sup> results for  $M_\infty = 2.5$  and  $\phi = 0^\circ$  with pitch (rotation) deflections. Results are shown for four sets of horizontal fin deflections:

- 1)  $\delta_{\text{CANARD}} = 0^\circ, \delta_{\text{TAIL}} = 0^\circ$
- 2)  $\delta_{\text{CANARD}} = 20^\circ, \delta_{\text{TAIL}} = 0^\circ$
- 3)  $\delta_{\text{CANARD}} = 0^\circ, \delta_{\text{TAIL}} = 20^\circ$
- 4)  $\delta_{\text{CANARD}} = 20^\circ, \delta_{\text{TAIL}} = -20^\circ$

The overall normal force, pitching moment and axial force characteristics are predicted well. The measured nonlinear characteristics of the pitching moment are indicated by the *MISL3* predictions. The predicted center of pressure is within one body radius of the measured value.

#### **TWO-FIN SET CONFIGURATION WITH FREE-ROLLING TAIL SECTION**

Figures 12, 13, and 14 present results for a canard-tail missile model.<sup>17</sup> Results for three test configurations are presented. For all configurations, the canards are in the  $\phi_{F1} = 0^\circ$  orientation (“+” orientation, designated C+). Three tail section orientations were tested:

- 1)  $\phi_{F2} = 0^\circ$  (“+” orientation, designated T+),
- 2)  $\phi_{F2} = 45^\circ$  (“X” orientation, designated Tx), and
- 3) tail section free to rotate (designated T-free).

The C+Tx configuration is depicted in Figures 12, 13, and 14. The model has a 3-caliber tangent-ogive nose and an overall body length of 15 diameters. The test Reynolds number was 2.0 million per foot.

The purpose of comparing to this experimental data was to investigate the predictive capabilities of the *MISL3* code and to gain insight into the aerodynamic characteristics of configurations with rolling tail sections. In this investigation, the *MISL3* code was used to: 1) estimate the static roll characteristics on the tail section under the influence of asymmetric canard vortices arising from roll control deflections, 2) estimate the roll damping characteristics of the tail section as a function of angles of attack, and 3) estimate the roll rate of the free-to-rotate tail section as a function of angle of attack.

Figure 12 compares measured<sup>17</sup> and predicted pitch plane aerodynamic characteristics for a Mach number of 1.7 with the horizontal canards deflected for roll control,  $\delta_{\text{ROLL}} = -5^\circ$  ( $\delta_{\text{ROLL}} = (\delta_{\text{C2}} - \delta_{\text{C4}})/2$ ). Measured and predicted results are shown for the C+T+ and C+Tx configurations. In addition, the measured data for the C+T-free configuration are also shown. The normal-force coefficient is predicted well for the C+T+ configuration. *MISL3* underpredicts the characteristics of the C+Tx configuration. The C+T+ pitching moment is in good agreement. The C+Tx pitching moment is overpredicted. The center of pressure is predicted within one body radius for both configurations except for small load conditions near  $\alpha_c = 0^\circ$ . The axial force is predicted well. The measured characteristics of the C+T-free configuration fall between the C+T+ and C+Tx characteristics.

Figure 13 compares measured and predicted rolling moment characteristics for the C+T+ and C+Tx configurations with canard roll control,  $\delta_{\text{ROLL}} = -5^\circ$ . In addition, the direct canard rolling moment predicted by *MISL3* is compared to the C+T-free measured results. The free-to-rotate tails do not pass a rolling moment to the main balance, except through bearing friction forces which are very small. It is seen in Figure 13 that the predicted direct roll control is in very good agreement with the measured C+T-free rolling moment. In addition, the rolling moments predicted for the C+T+ and C+Tx configurations agree well with data up to  $4^\circ$  angle of attack and have the correct trends above  $4^\circ$ .

The rolling moment is difficult to predict because it is dominated by the canard and body shed vortices influencing the tail fins. This is the classical induced roll. For these configurations, the induced tail fin rolling moment opposes the direct canards control and actually causes the rolling moment to be negative.

Figure 14 depicts the predicted crossflow velocity fields at the leading edge of the tail fin section for angles of attack of 0, 4, 8, and  $12^\circ$ . For  $\alpha_c = 0^\circ$ , Figure 14(a), it is seen that the canard vortices produce a counterclockwise swirling flow which produces the negative induced rolling moment on the tail fin section as seen in Figure 13. For  $\alpha_c = 4^\circ$ , Figure 14(b), the effects of the vortex shed from the right canard vortex is not apparent because it is lightly loaded ( $\alpha_c + \delta_{\text{C2}} = -1^\circ$ ). There is a stronger vortex on the left side corresponding to  $\alpha_c + \delta_{\text{C4}} = +9^\circ$ . The flow field is asymmetric and results in a negative induced tail fin section rolling moment. The results for  $\alpha_c = 8^\circ$ , Figure 14(c), show a large vortex from the left canard and a weaker one from the right canard. The higher angle of attack results in the vortices tracking further

upwards. There is still an asymmetric flow field which produces a negative tail section rolling moment for both the C+T+ and C+Tx configurations. Figure 14(c) also indicates the beginning of the body shed vorticity modeled by *MISL3*.

When  $\alpha_c = 12^\circ$ , Figure 14(d), the canard vortices have tracked to positions above the tail fin region, and significant body shed vorticity is present. The induced rolling moment on the tail fin section is small for this angle of attack for both the C+T+ and C+Tx configurations, but it has a positive slope, Figure 13. Above  $12^\circ$  angle of attack, the predicted induced rolling moment from the tail fins is positive. The experimental data shows this behavior to a lesser extent. In the prediction, this arises from the asymmetric body vorticity (produced due to asymmetric canard vorticity). The left-side body vorticity is weaker than the right-side; the result is an induced positive roll on the tail fins for both the C+T+ and C+Tx configurations. This is similar, but opposite, to the results at lower angles of attack with asymmetric canard vortices. Further insight is gained from these crossflow velocity predictions when the variation of tail section rolling moment as a function of interdigitation angle is discussed later in this section in connection with Figure 15(a).

*MISL3* can be used to estimate the aerodynamic characteristics of the rolling tail section including tail section roll rate as follows. The roll equation of motion for the tail section as a function of time  $t$  is:

$$T = T_{\text{AF}}(t) + T_{\text{AD}}(t) + T_{\text{BF}}(t) = I_X(dp/dt) \quad (3)$$

where  $T$  is torque,  $I_X$  is the roll moment of inertia of the tail section, and the subscripts designation are:

- AF - aerodynamic forcing,
- AD - aerodynamic damping, and
- BF - bearing friction (or brake force).

The time-dependent aerodynamic forcing torque on the tail fins,  $T_{\text{AF}}(t)$ , is caused by the aerodynamic fin forces which are dependent on the angle of attack and the fin section roll angle,  $\phi_{\text{F2}}$ . The aerodynamic damping torque,  $T_{\text{AD}}(t)$ , is dependent on the tail section roll rate and the angle of attack. The third torque,  $T_{\text{BF}}$ , can be used to model bearing friction and/or braking torque. The effects of braking torque and the simulation of the tail roll behavior through integration of the Eqn. (3) will be addressed in a future effort.

Because the current version of *MISL3* does not integrate the roll equation of motion of the free-to-rotate tail section, the characteristics must be estimated based on static characteristics and calculated roll damping

characteristics. The analysis of Falanga<sup>18</sup> is followed. For steady-state conditions (constant roll rate, no variance with  $\phi_{F2}$ ), the sum of the moments must be zero.

$$\sum \text{moments} = M_{AF} + M_{AD} + M_{BF} = 0 \quad (4)$$

$$\begin{aligned} \text{Substituting } M_{AF} &= C_l q_\infty S_R l_R \text{ and} \\ M_{AD} &= C_{lp} (p l_R / 2V_\infty) q_\infty S_R l_R \end{aligned}$$

into Eqn. (4) and solving for the roll rate  $p$ , yields:

$$\frac{p l_R}{2V_\infty} = -\frac{C_l}{C_{lp}} \left(1 + \frac{M_{BF}}{M_{AF}}\right) \quad (5)$$

For cases where the bearing torque is much smaller than the aerodynamic torque, the roll rate can be estimated as follows:

$$\frac{p l_R}{2V_\infty} = -\frac{C_l}{C_{lp}} \quad \text{for } M_{BF} \ll M_{AF} \quad (6)$$

For a high quality bearing, this assumption is valid.

For the canards deflected  $\pm 5^\circ$  for roll control ( $\delta_{\text{ROLL}}$ ), Figure 15(a) shows the predicted static rolling-moment coefficient of the tail fin section as a function of tail fin set roll angle  $\phi_{F2}$ . Results are shown for angles of attack of 0, 4, 8, and 12°. It is seen that the tail fin rolling moment is negative (right fin up) for angles of attack below 8°. This is apparent in the flow field predictions shown in Figures 14(a)-14(c) which show partially counterclockwise flow fields for  $\alpha_c = 0$  and 4°. Above 4° angle of attack, a significant cyclic variation in  $C_l$  develops, Figure 15(a). For 12°, the rolling moment variation is cyclical and changes sign. The slope of  $C_l$  with respect to  $\phi_{F2}$  at the zero crossings is such that the tail section would “lock-in” to a zero roll rate. These zero crossings occur at approximately 45° intervals.

In order to estimate the tail fin roll rate using Eqn. (6),  $C_l$  and  $C_{lp}$  must be estimated.  $C_l$  is estimated as the mean  $C_l$  with respect to  $\phi_{F2}$  (see Figure 15(a)). This mean  $C_l$  is plotted as a function of angle of attack in Figure 15(b). The roll damping coefficient,  $C_{lp}$ , is estimated by running *MISL3* with a nonzero roll rate (tail fins only) and computing  $C_{lp}$  by finite difference. It was found that  $C_{lp}$  was constant for the range of roll rates under investigation (that is,  $C_l$  is linear with respect to  $p$ ). However, there is a dependence on angle of attack as shown in Figure 15(c).

The tail fin roll rate is then estimated as  $-C_l/C_{lp}$  (Eqn. (6), and converted to rpm) and is shown in Figure 15(d). While the magnitude of the roll rate is underpredicted, the trends are predicted well. *MISL3* predicts that the mean  $C_l$  in Figure 15(b) becomes positive above 12° angle of attack. However, the characteristics of the rolling moment predicted with respect to  $\phi_{F2}$  are such that the tail fins “lock-in” to a zero roll rate around 12°. The experimental results indicate that this happens at 14°. The *MISL3* results are dependent on the prediction of mean  $C_l$  and  $C_{lp}$  for the tail section. These quantities are difficult to predict accurately, especially when they are influenced by upstream asymmetric vorticity. The sensitivity of the estimated quantities to various parameters should be studied further.

It is seen that *MISL3* provides a reasonable estimate of the roll rate characteristics of a free-to-roll tail section under the influence of the asymmetric flow field associated with canard roll control as a function of angle of attack.

## CONCLUSIONS

A fast and efficient aerodynamic prediction program, *MISL3*, has been developed for missiles at speeds up to  $M_\infty = 5$  and at angles of attack up to 90°. The code is applicable to configurations with up to three fin sections. The body can have conical changes in diameter aft of the nose. Configuration roll angle and interdigitation angle between fin sets are arbitrary. The *MISL3* code can also include effects of angular rates and nonuniform flow fields. The basic underlying methodology includes a systematic fin-on-body data base, the equivalent angle of attack concept, models for the nonlinear effects of fin wake and body-shed vorticity, and analytical extensions for geometric and flow conditions outside the range of application of the fin-on-body data base.

This paper describes new and unique applications to configurations with tandem controls and a free-rolling tail section as well as to conventional airframe shapes. The extensive comparisons to experimental aerodynamic data include longitudinal and lateral aerodynamic characteristics. In general, the predicted aerodynamic characteristics are in good to excellent agreement with the experimental data. On the basis of the comparisons described in this paper, the *MISL3* code should be used by applied aerodynamicists involved in preliminary design of conventional missile airframes as well as design of missiles with advanced controls and special features such as a rolling tail section.

## ACKNOWLEDGMENTS

The *MISL3* missile aerodynamics prediction code is the latest development of a set of codes (*MISSILE1*, etc.) originally funded by ONR in 1972. Later versions were funded by NAVAIR. After NEAR used its own IR&D to develop its proprietary version, NAWCWPNS licensed the resulting code with special added functionalities. NEAR gratefully acknowledges Mr. E. L. Jeter, Code 476F00D NAWCWPNS China Lake, CA, for his continued support of the *MISL3* code. NEAR would also like to thank Mr. Jerry M. Allen of NASA/LaRC for his assistance in obtaining the Tandem-Control wind tunnel data.

## REFERENCES

1. Lesieutre, D. J., Love, J. F., and Dillenius, M. F. E., "*MISL3*-November 2000 Aerodynamic Analysis for Finned Vehicles with Axisymmetric Bodies," NEAR TR 561, Nov. 2000.
2. Lesieutre, D. J., Love, J. F., and Dillenius, M. F. E., "High Angle of Attack Missile Aerodynamics Including Rotational Rates - Program *M3HAX*," AIAA 96-3392, Jul. 1996.
3. Lesieutre, D. J., Love, J. F., and Dillenius, M. F. E., "*M3HAX* Aerodynamic Analysis for Finned Vehicles with Axisymmetric Bodies," NEAR TR 493, Feb. 1996.
4. Lesieutre, D. J., Dillenius, M. F. E., and Whittaker, C. H., "*M3F3CA* Aerodynamic Analysis for Finned Vehicles with Axisymmetric Bodies," NEAR TR 424, May 1991.
5. Lesieutre, D. J., Mendenhall, M. R., Nazario, S. M., and Hensch, M. J., "Prediction of the Aerodynamic Characteristics of Cruciform Missiles Including Effects of Roll Angle and Control Deflection," NEAR TR 360, Revised Aug. 1987.
6. Lesieutre, D. J., Mendenhall, M. R., and Dillenius, M. F. E., "Prediction of Induced Roll on Conventional Missiles with Cruciform Fin Sections," AIAA 88-0529, Jan. 1988.
7. Allen, J. M., Shaw, D. S., and Sawyer, W. C., "Analysis of Selected Data From The Triservice Missile Data Base," AIAA 89-0478, Jan. 1989.
8. Jorgensen, L. H., "Prediction of Static Aerodynamic Characteristics for Slender Bodies Alone and with Lifting Surfaces to Very High Angles of Attack," NASA TR R-474, Sep. 1977.
9. Aiello, G. F. and Bateman, M. C., "Aerodynamic Stability Technology for Maneuverable Missiles. Vol. I, Configuration Aerodynamic Characteristics," AFFDL-TR-76-55, Vol. I, Mar. 1979.
10. Packard, J. D. and Miller, M. S., "Assessment of Engineering-Level Codes for Missile Aerodynamic Design and Analysis," AIAA 2000-4590, Aug. 2000.
11. Riley, D. R., "Some Effects of Nose Deflection and Number of Tail Fins on the Aerodynamic Characteristics in Pitch and Sideslip of a Wingless Missile at a Mach Number of 3.11," NASA TM X-270, Aug. 1965.
12. Trescot, C. D., Jr., Foster, G. V., and Babb, C. D., "Effect of Fin Planform on the Aerodynamic Characteristics of a Wingless Missile with Aft Cruciform Controls at Mach 1.60, 2.36, and 2.86," NASA TM X-2774, Jul. 1973.
13. Corlett, W. A. and Richardson, C. S., "Effect of First-Stage Geometry on Aerodynamic Characteristics in Pitch of Two-Stage Rocket Vehicles from Mach 1.57 to 2.86," NASA TN D-2709, Mar. 1965.
14. Robinson, R. B., "Effects of Body and Fin Deflection on the Aerodynamic Characteristics in Pitch of a 0.065-Scale Model of a Four-Stage Rocket Configuration at Mach Numbers of 1.41 and 1.82," NASA TN D-37, Sep. 1959.
15. Jorgensen, L. H. and Nelson, E. R., "Experimental Aerodynamic Characteristics for Slender Bodies with Thin Wings and Tail at Angles of Attack from 0° to 58° and Mach Numbers from 0.6 to 2.0," NASA TM X-3310, Mar. 1976.
16. The Tandem-Control Data were taken by A. B. Blair, Jr., NASA LaRC.
17. Blair, A. B., Jr., "Wind-Tunnel Investigation at Supersonic Speeds of a Remote-Controlled Canard Missile With a Free-Rolling-Tail Brake Torque System," NASA TP 2401, Mar. 1985.
18. Falanga, R. A., "Supersonic Investigation of a Spinning and Nonspinning Model of a Cajun (or Apache) Rocket Vehicle With Roll-Control Tabs," NASA TN D-2576, Jan. 1965.

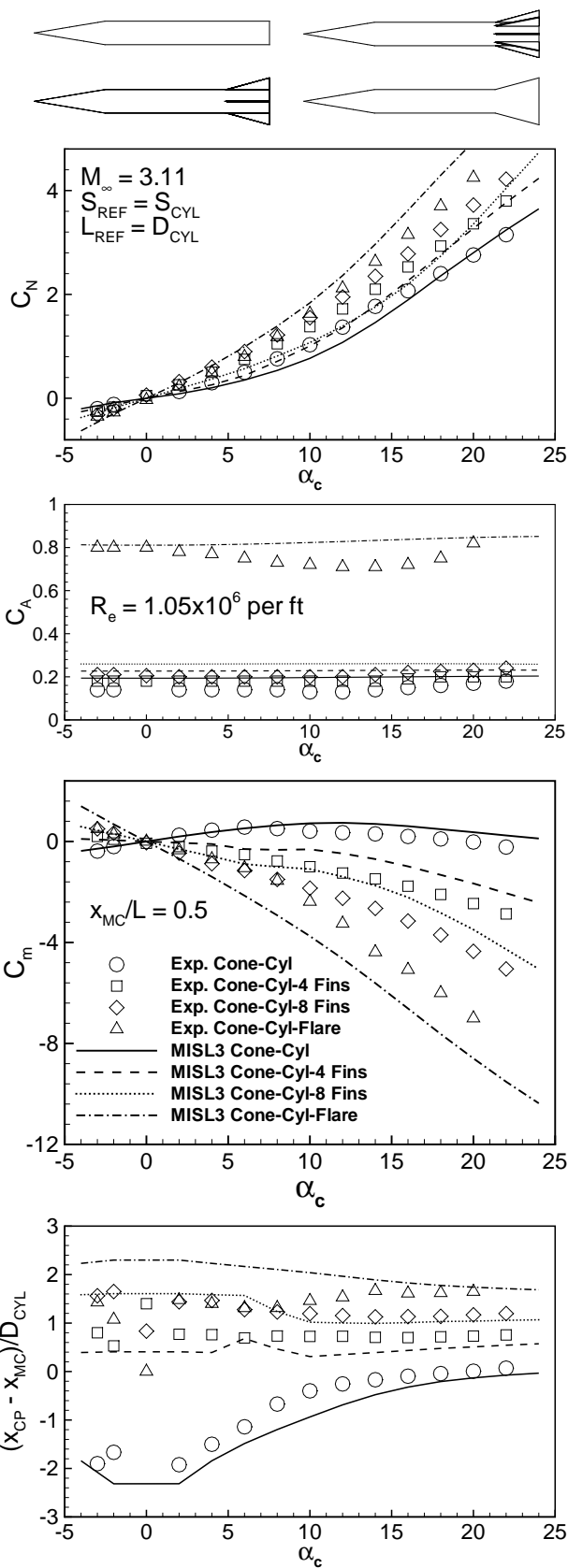


Figure 1.- Comparison of measured and predicted aerodynamic characteristics of four conecylinder fin and flare configurations, Ref. 11.

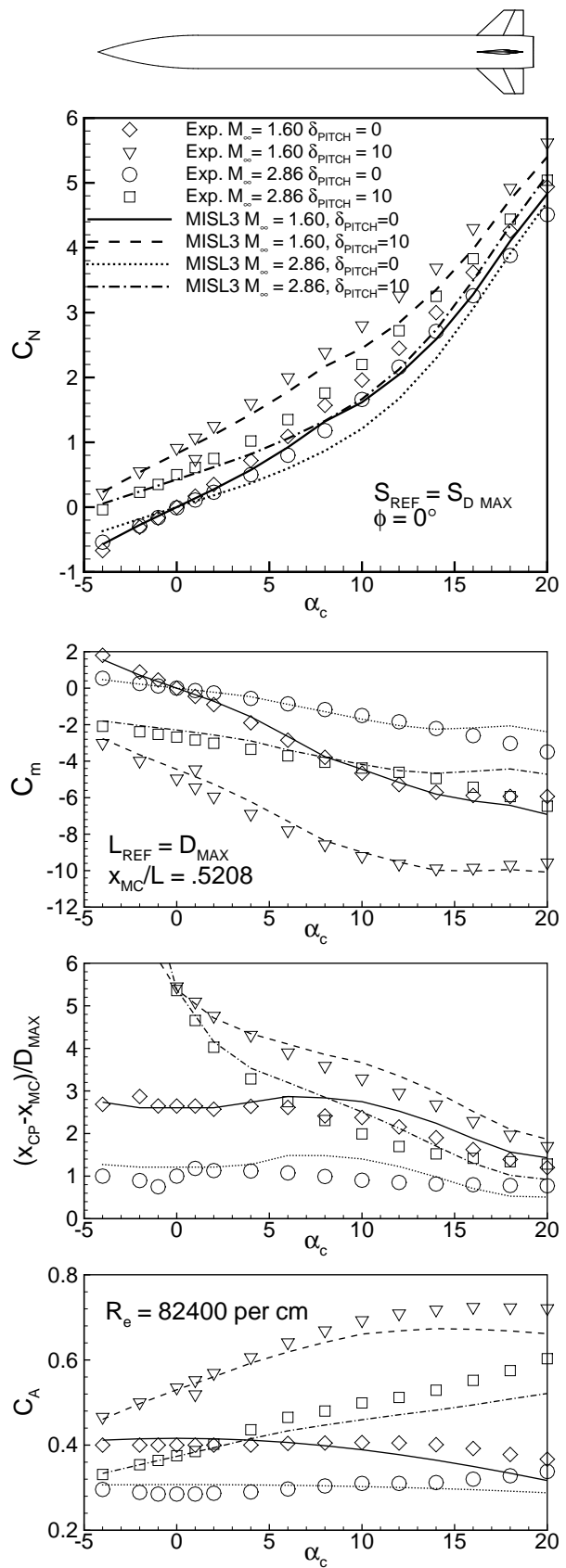


Figure 2.- Comparison of measured and predicted aerodynamic characteristics, tail pitch control,  $\phi = 0^\circ$ ,  $M_\infty = 1.60, 2.86$ , Ref. 12.

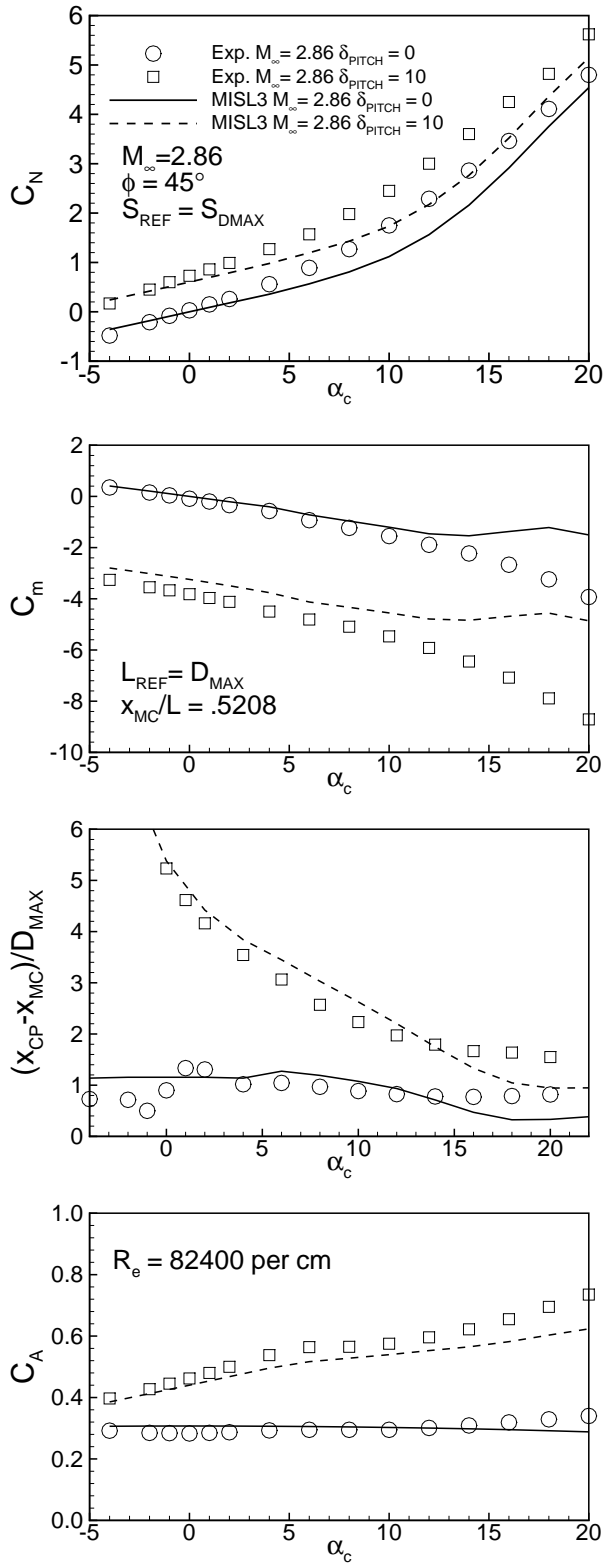
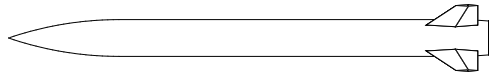


Figure 3.- Comparison of measured and predicted aerodynamic characteristics, tail pitch control,  $\phi = 45^\circ$ ,  $M_\infty = 2.86$ , Ref. 12.

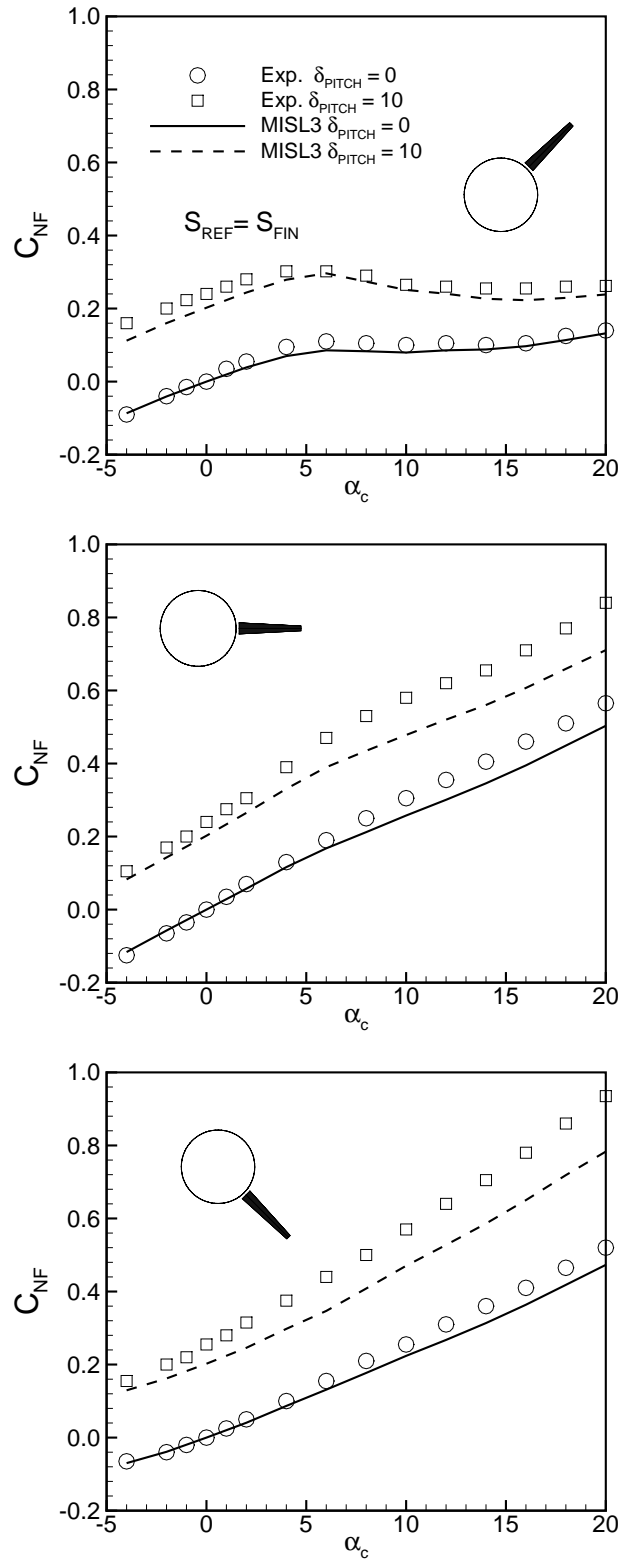


Figure 4.- Comparison of measured and predicted fin aerodynamic characteristics, tail pitch control,  $M_\infty = 2.86$ , Ref. 12.

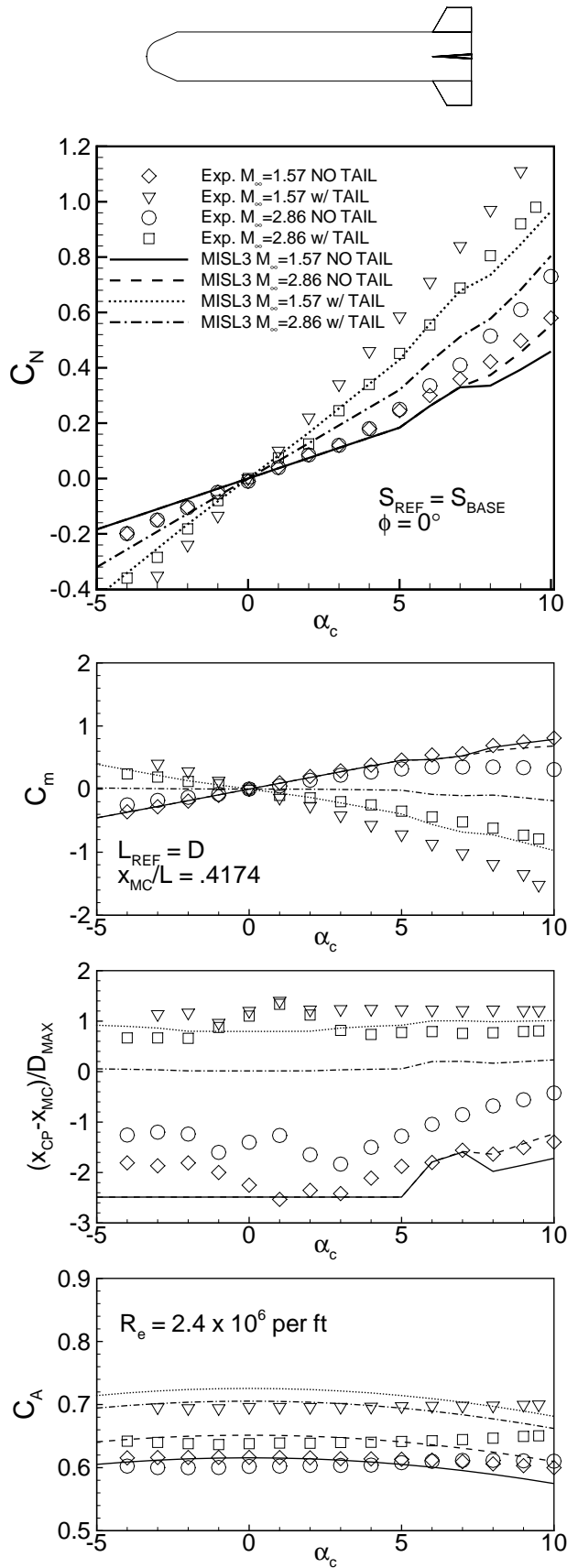


Figure 5.- Comparison of predicted and measured aerodynamic characteristics showing effect of the tail fins,  $\phi = 0^\circ$ ,  $M_\infty = 1.57, 2.86$ , Ref 13.

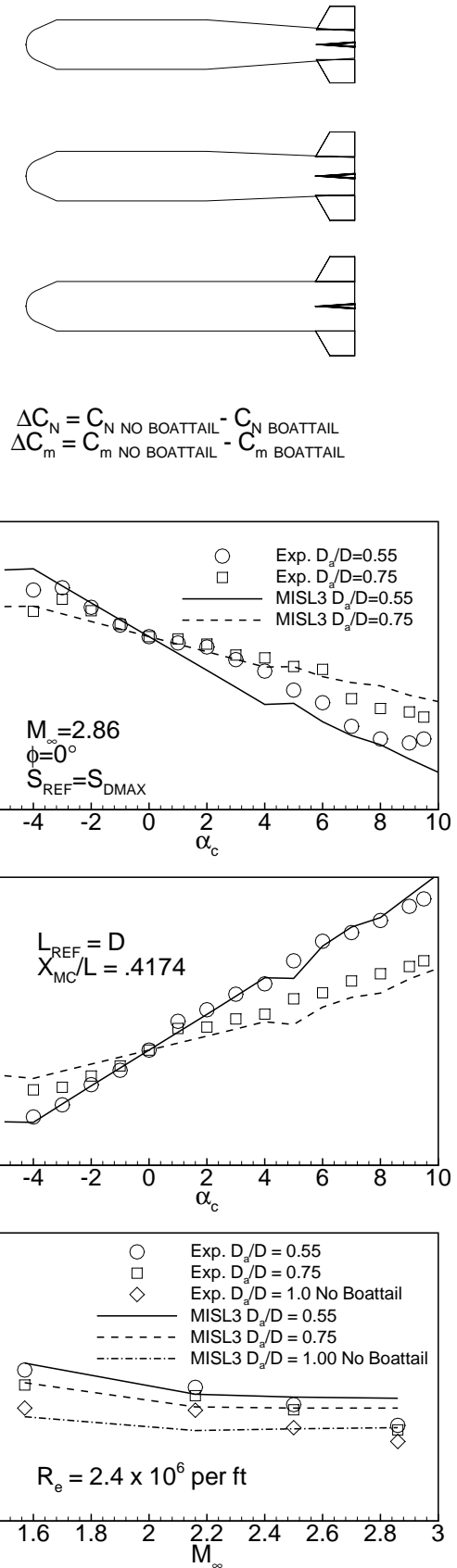


Figure 6.- Comparison of predicted and measured incremental aerodynamic characteristics and axial force coefficients for various boattail ratios,  $\phi = 0^\circ$ ,  $M_\infty = 2.86$ , Ref. 13.

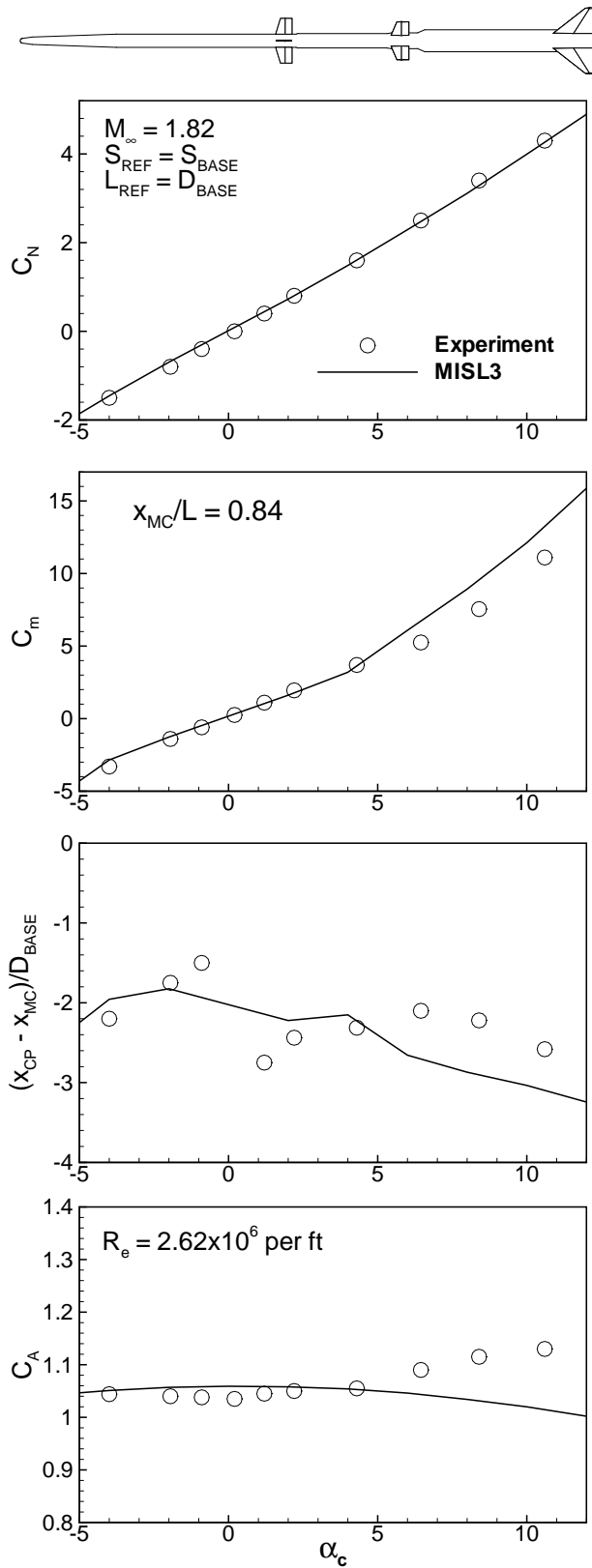


Figure 7.- Comparison of predicted and measured aerodynamic characteristics for a flared body with three fin sets and interdigation, Ref. 14.

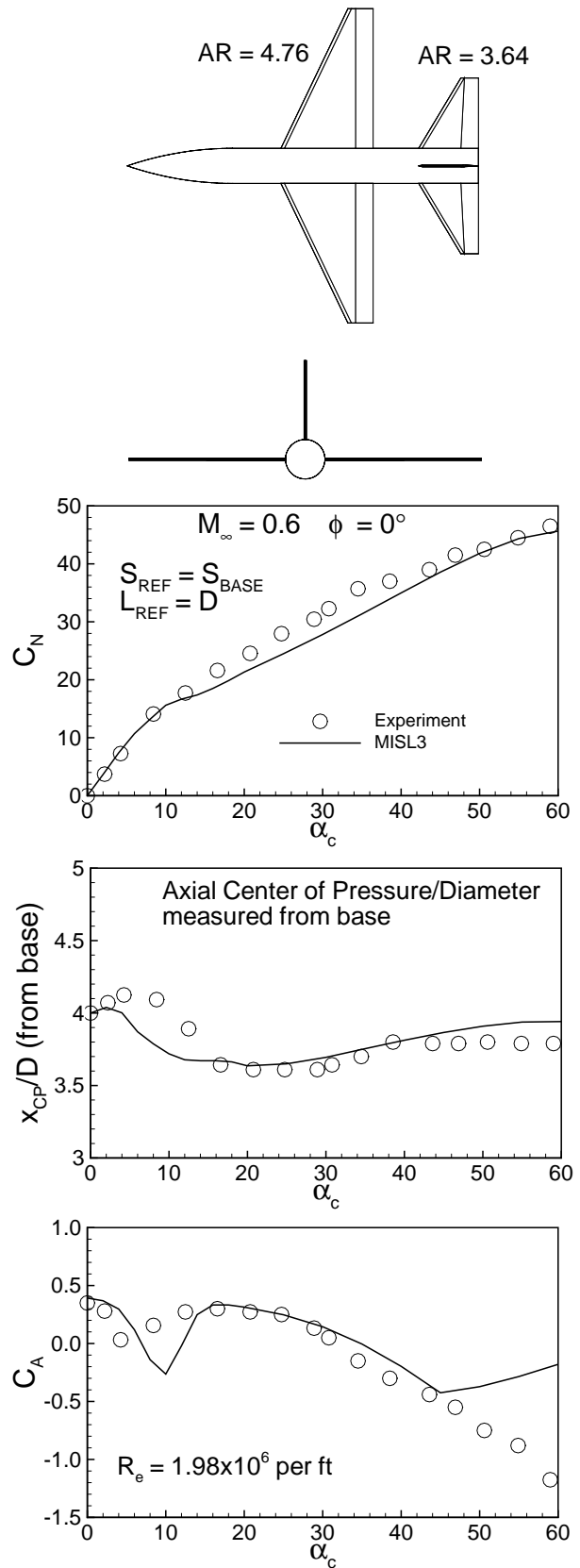


Figure 8.- Comparison of predicted and measured aerodynamic characteristics of a high aspect ratio wing configuration, Ref. 15.

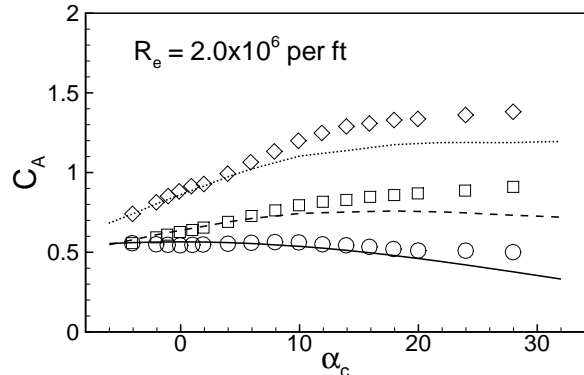
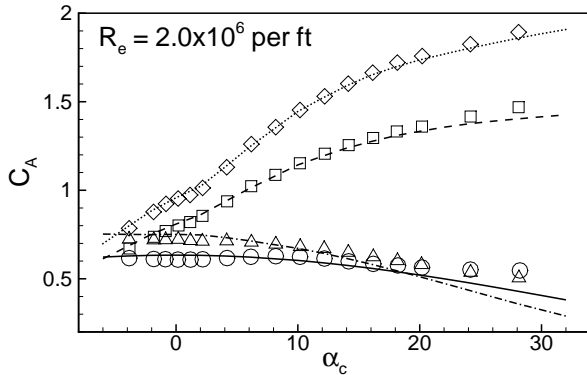
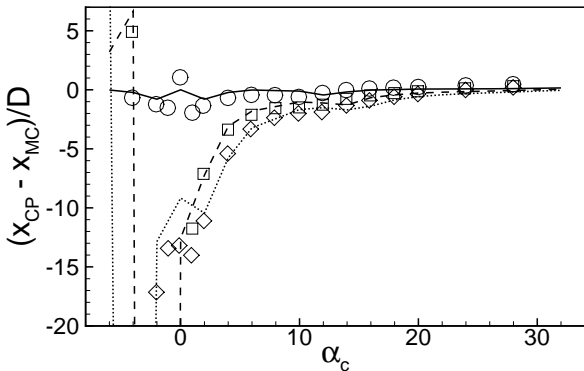
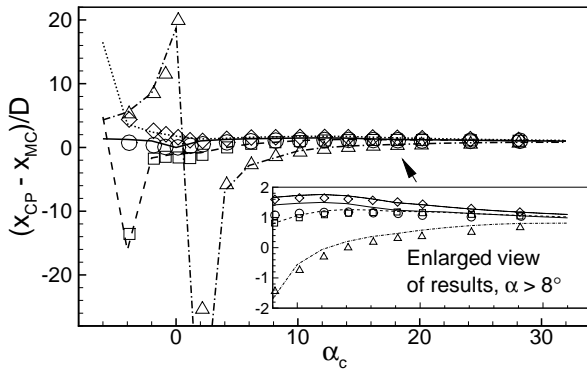
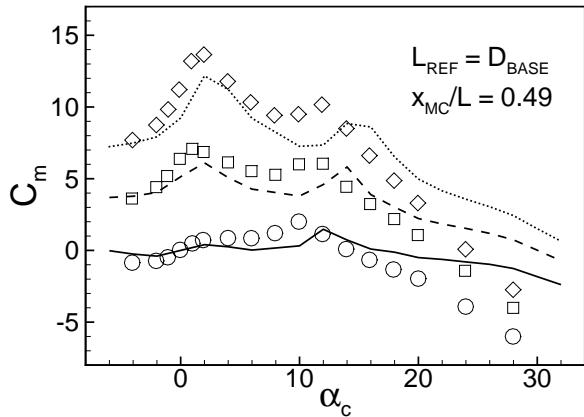
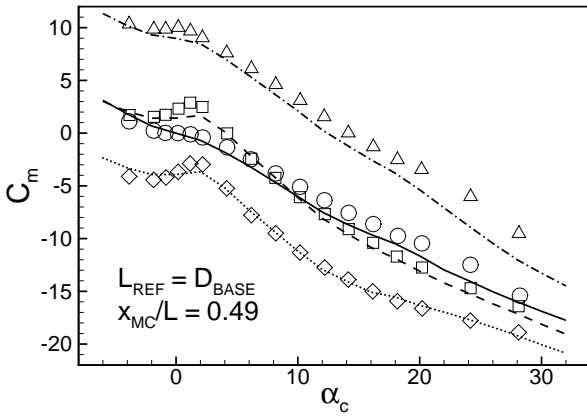
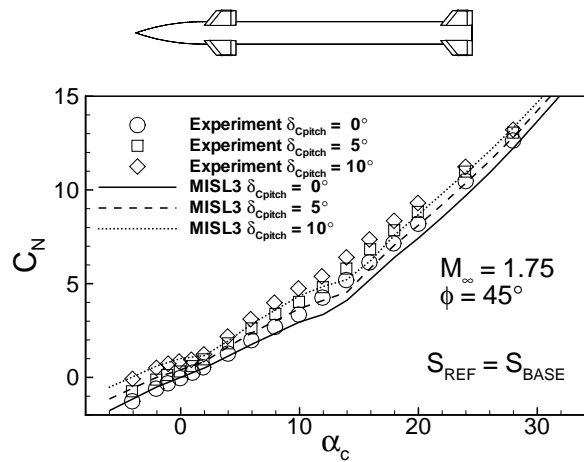
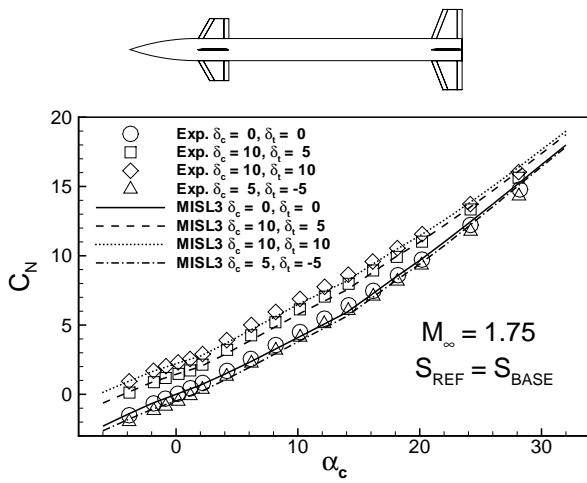


Figure 9.- Comparison of measured and predicted aerodynamic characteristics for a tandem-control missile;  $M_\infty = 1.75$ ,  $\phi = 0^\circ$ , Ref. 16.

Figure 10.- Comparison of measured and predicted aerodynamic characteristics, canard pitch control for  $\phi = 45^\circ$ ,  $M_\infty = 1.75$ , Ref. 16.

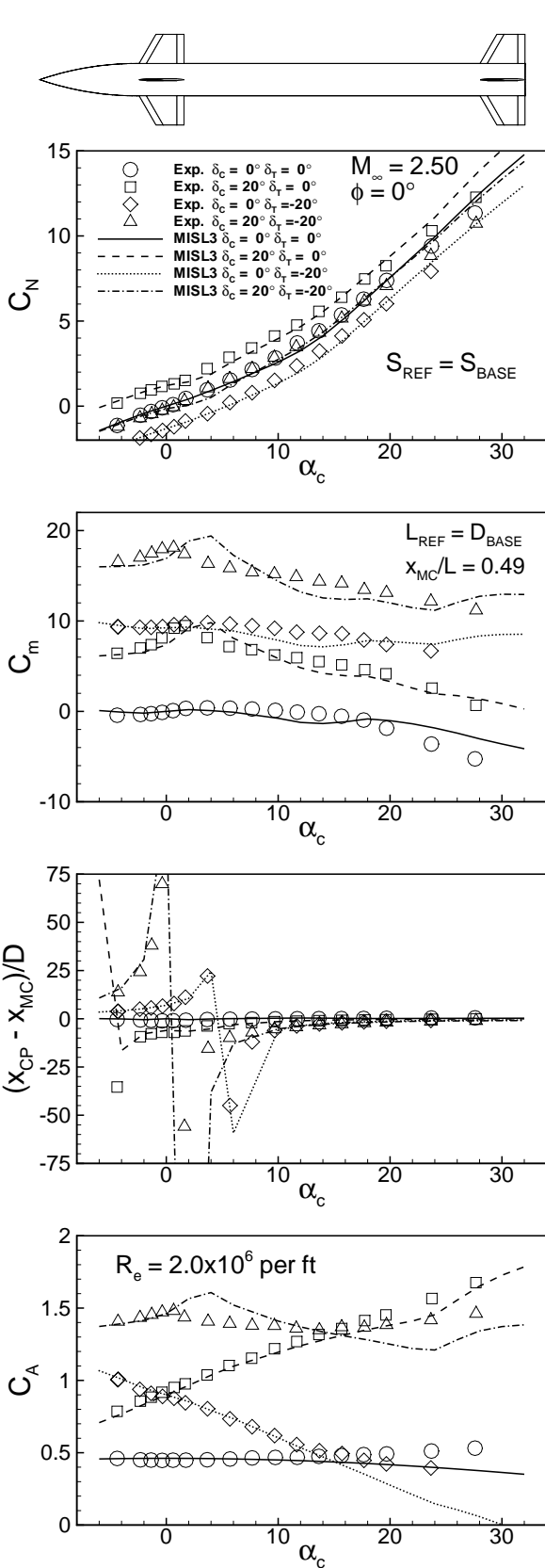


Figure 11.- Comparison of measured and predicted aerodynamic characteristics for a tandem-control missile;  $M_\infty = 2.5$ ,  $\phi = 0^\circ$  Ref. 16.

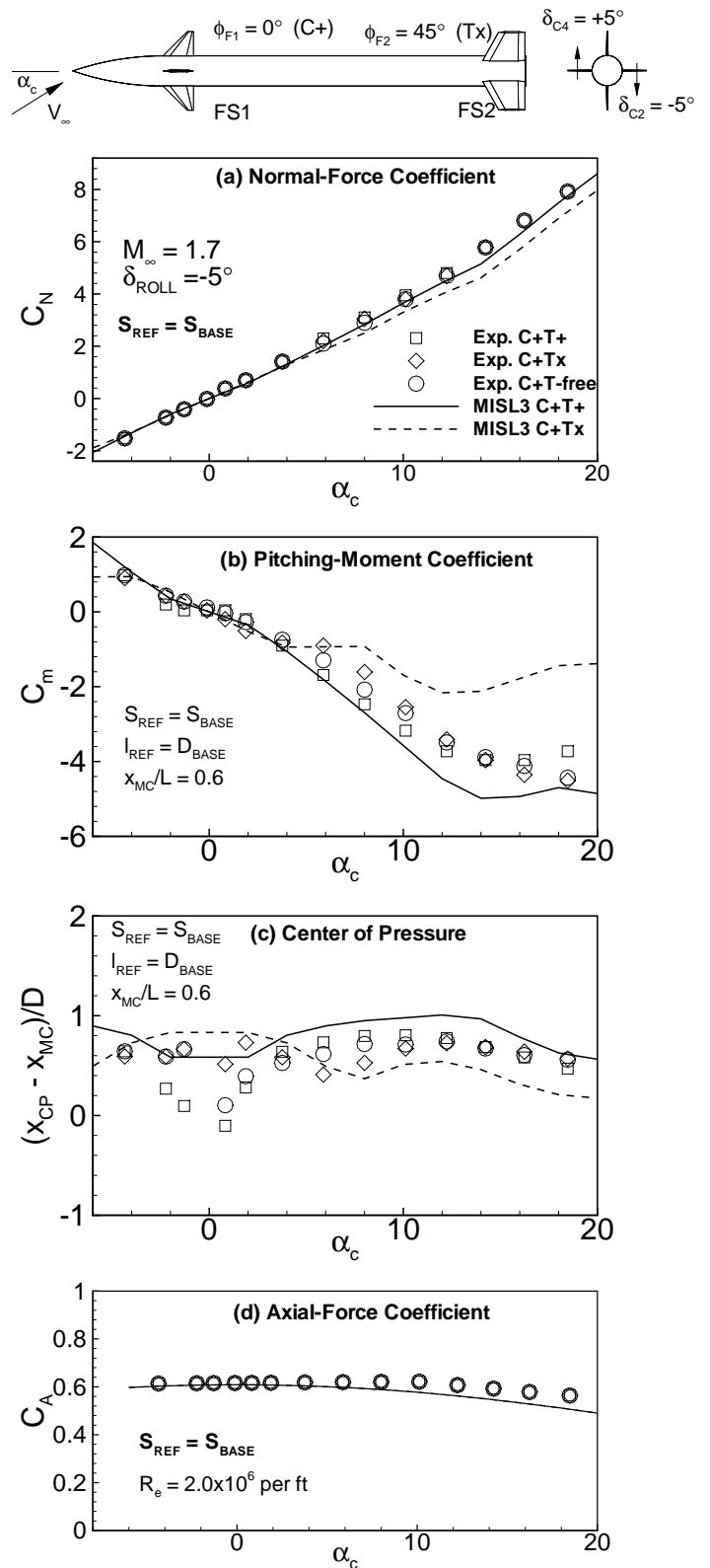


Figure 12.- Comparison of predicted and measured pitch-plane aerodynamic characteristics of a canard-tail configuration (Ref. 17) with: 1) tails inline with canards (C+T+), 2) tails interdigitated  $45^\circ$  (C+Tx), and 3) tails free to rotate (C+T-free).

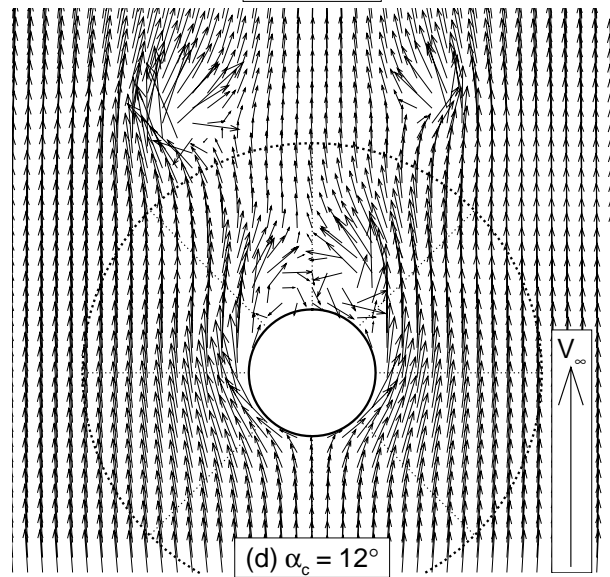
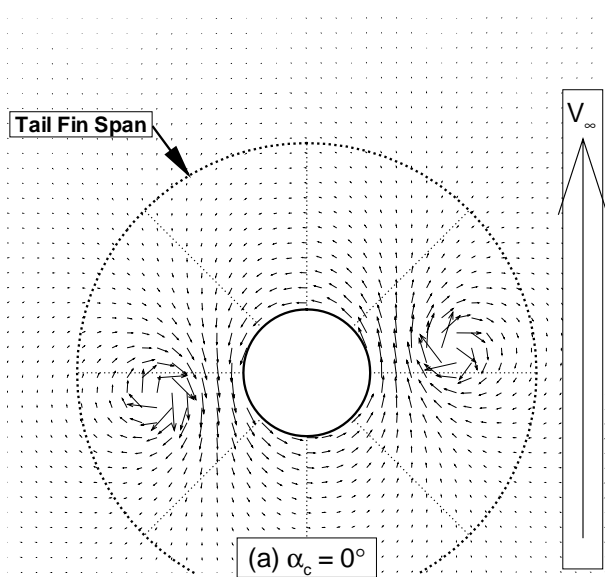
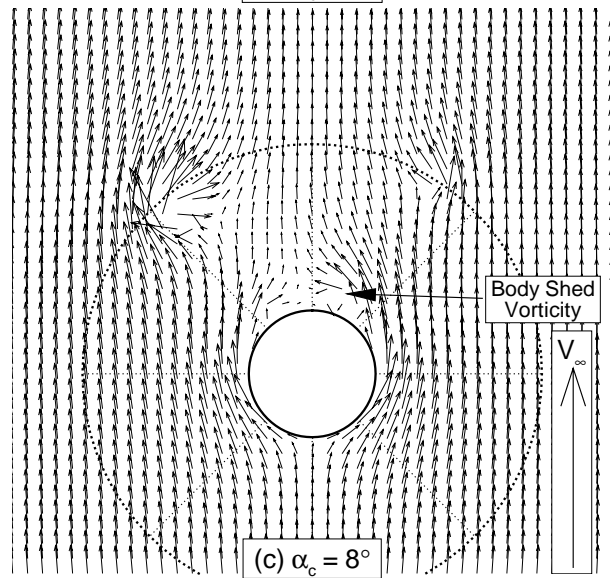
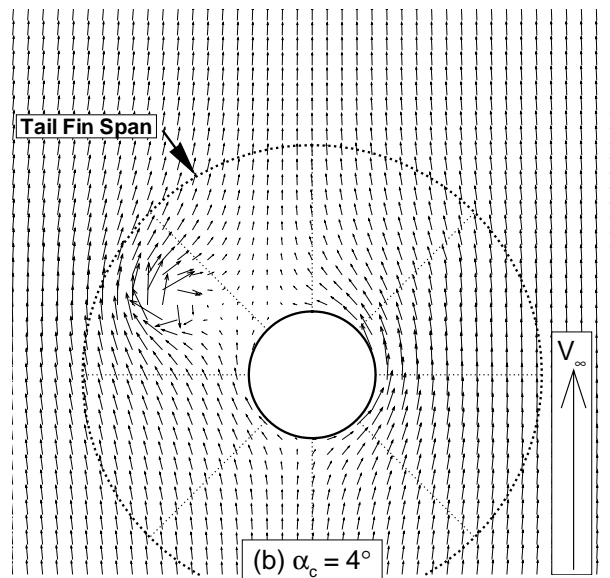
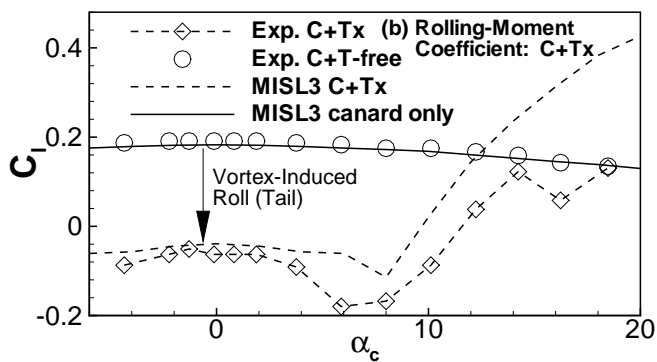
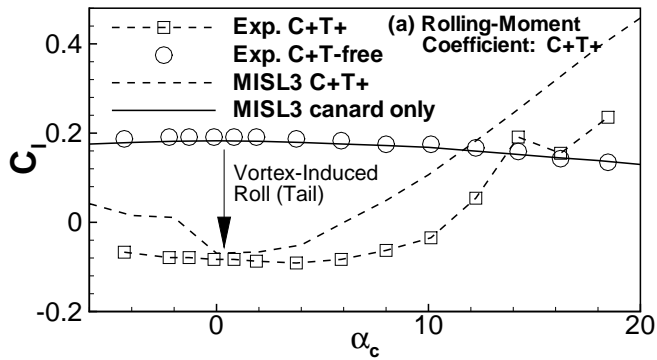
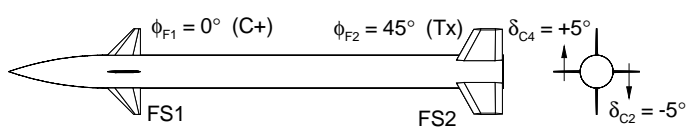


Figure 13.- Comparison of predicted and measured rolling-moment aerodynamic characteristics of a canard-tail configuration (Ref. 17) with:  
 1) tails in line with canards (C+T+),  
 2) tails interdigitated 45° (C=Tx), and  
 3) tails free to rotate (C+T-free).

Figure 14.- Predicted crossflow velocity fields at the leading edge of the tail fin section,  $M_\infty = 1.7$ ,  $\delta_{C2} = -5^\circ$ ,  $\delta_{C4} = +5^\circ$ .

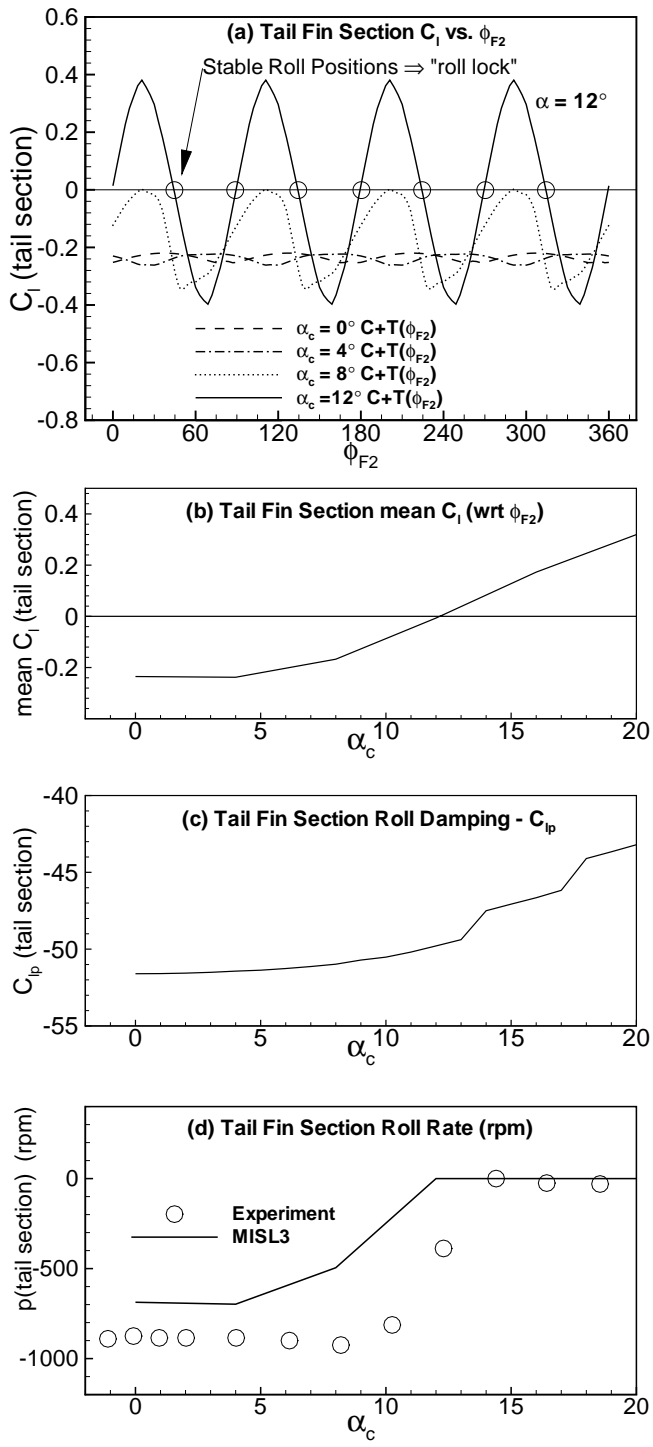
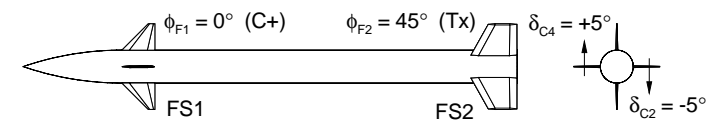


Figure 15.- Comparison of predicted and measured tail section aerodynamic characteristics,  $M_\infty = 1.7$ ,  $\phi = 0^\circ$ ,  $\delta_{C2} = -5^\circ$ ,  $\delta_{C4} = +5^\circ$ , tail free to rotate, Ref. 17.